Journal of Applied Geophysics 114 (2015) 191–201

Contents lists available at ScienceDirect

Journal of Applied Geophysics

journal homepage: www.elsevier.com/locate/jappgeo

Wideband impedance spectroscopy from 1 mHz to 10 MHz by combination of four- and two-electrode methods

J. Volkmann *, N. Klitzsch

Applied Geophysics and Geothermal Energy, E.ON Energy Research Center, RWTH Aachen University, Mathieustraße 10, 52074 Aachen, Germany

ARTICLE INFO

Article history:
Received 2 October 2014
Received in revised form 19 December 2014
Accepted 14 January 2015
Available online 21 January 2015

Keywords:
Wideband impedance spectroscopy
Electrical measurement and processing
Spectral induced polarization (SIP)

ABSTRACT

Impedance Spectroscopy (IS) measurements allow to study a wide range of polarization mechanisms associated with different frequency ranges. Experimental devices usually cover limited frequency ranges with sufficient accuracy. We propose (a) a combination of four-electrode and two-electrode devices and (b) a data combination and mutual verification procedure using the actual sample under test. Hereby, we cover a frequency range from 1 mHz to 10 MHz. The data combination relies on the precondition that any dispersive disturbance decayed at some mutual point within an overlapping frequency range between 1 Hz and 45 kHz. We validate our data combination procedure by IS measurements on simple reference systems and comparison with widely accepted model functions, e.g. the complex refractive index model (CRIM) for high frequency behavior and Kramers–Kronig relations in terms of data consistency. In this respect, our suggested processing approach is superior to two selected alternative approaches. We successfully adapt typical empirical model functions, e.g. multi-Cole–Cole, to the resulting wideband data to show that they are fully applicable for further data analysis.

1. Introduction

Impedance Spectroscopy (IS) is an electrical measurement technique which takes advantage of the frequency dependence of alternating current responses of a given sample. Since it can be applied to a wide range of different materials, impedance measurements are a common technique in an equally wide range of material sciences (McKubre et al., 1987). In geophysics, it is usually called Spectral Induced Polarization (SIP) and used for laboratory analyzes as well as in the field, where it mainly serves imaging purposes (e.g. Kemna et al., 2012).

Impedance Spectroscopy (IS) data of water saturated rocks are subject to a range of polarization mechanisms, depending on the studied frequency range. In raw order of increasing frequency up to 10 MHz, we find Stern layer polarization (Schwarz, 1962; Revil and Florsch, 2010), possibly going together with membrane polarization (Marshall and Madden, 1959; Titov et al., 2002; Volkmann and Klitzsch, 2010; Bücker and Hördt, 2013) effects, followed by Maxwell–Wagner polarization and orientational polarization of water molecules (Maxwell, 1873; Wagner, 1914; Hanai, 1960; Chelidze and Guegen, 1999). Additionally, electrode polarization can occur in the presence of conductive minerals (Pelton et al., 1978). In detail, the frequency ranges of the individual processes often considerably overlap (Revil, 2013), which makes a discrimination difficult at least at the limits of a particular frequency range. An example is given in Fig. 1, where data interpretation approaches would strongly depend on the assumed behavior outside of the measured frequency range.

Moreover, the polarization effects at different frequency ranges are caused by different physical mechanisms, e.g. diffusion or space charge separation, and tend to arise in the presence of particular micro-geometric conditions. Thus, they offer different deducible rock properties (Slater, 2007; Chelidze and Guegen, 1999; Cosenza et al., 2009), beyond DC (Archie, 1942) or single frequency AC (Börner et al., 1996) methods.

Thus, to cover the majority of these effects within a particular measurement and allow a reliable interpretation, it is desirable to study a relatively wide frequency range with IS measurements.

Unfortunately, most measurement setups are designed to produce most accurate data only in a limited frequency range, whereas this accuracy rapidly decreases outside of the optimal frequency range (cf. technical data of arbitrary IS instrument). In addition, impedance measurement systems have some major limitations, even if measurement electronics are state of the art. For example, in two-electrode measurements the electric connection between sample and measurement electrodes can introduce transfer impedance effects depending on a variety of parameters and cause frequency dependent disturbance from lowest frequencies up to the kHz-range. Using a four electrode setup, electromagnetic coupling between different elements of the setup, e.g. wires,

---

* Corresponding author.
E-mail address: jvolkmann@eonerc.rwth-aachen.de (J. Volkmann).

http://dx.doi.org/10.1016/j.jappgeo.2015.01.012

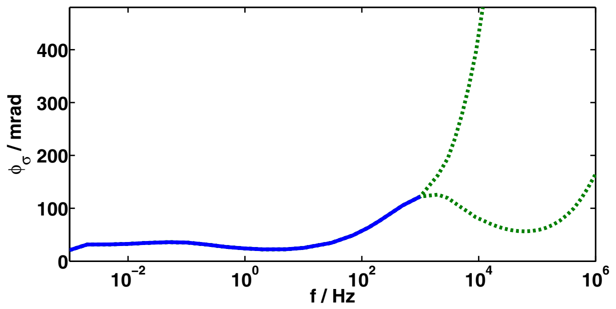

Fig. 1. IS phase spectrum, measured up to 1 kHz (blue line). Various continuations are possible (two examples shown as dashed green line) and indicate different polarization mechanisms being responsible for the phase increase above 1 Hz.

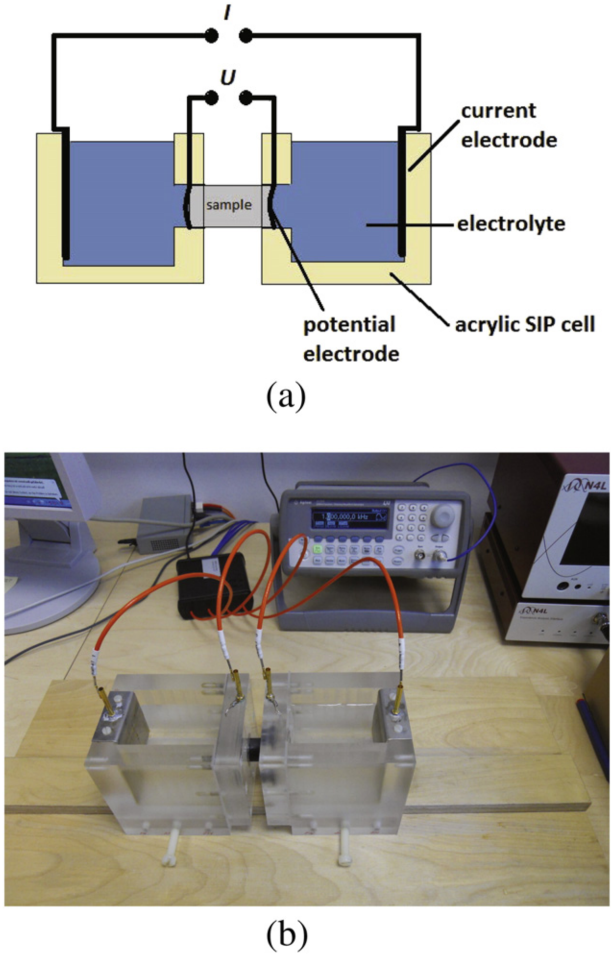

Fig. 2. (a): Design of the used four-electrode cell; (b): image of the four-electrode cell.

can lead to frequency dependent errors, especially at high frequencies above 100 Hz. Additional errors may arise, e.g. from sample handling, temperature dependent conductivity drift or limited instrument accuracy. Thus, for one particular setup, it is rarely possible to avoid error-prone data, especially at the limits of its optimal frequency range.

Several authors propose a subsequent data correction using an approximated error description and thereby try to extend the valid frequency range (e.g. Kavian, 2011).

We propose procedures for obtaining wideband IS data in a frequency range from 1 mHz up to 10 MHz without necessity for such subsequent error model development. Therefore, we use two different devices which are suitable for different, but overlapping frequency ranges, following the approach of Lockner and Byerlee (1985) to combine four- and two-electrode methods. We develop a work flow for a consistent combination of the individual data sets, not requiring previous characterization of the disturbing processes. This advantage accrues from the possibility of mutual validation and/or correction in the course of the data combination procedure and forms the core of the proposed approach.

In the following, we first introduce our hardware and test samples. Then, we describe the data combination and correction procedure, leading to a wideband data set. We introduce alternative approaches for comparison with the proposed method. Afterwards, we describe our data quality estimation for the combined data using established model functions and relations. Finally, we show combined wideband data sets for different rock types to show a wide range of applicability of our method. Moreover, we apply and discuss alternative data combination approaches for comparison with the proposed method.

2. Hardware and samples

We propose a combination of two different IS setups, covering the frequency range of 1 mHz to 10 MHz. The first one is used in the frequency range from 1 mHz to 45 kHz and adapted to lower frequency experimental requirements. The second setup is used in the frequency range from 1 Hz to 10 MHz, thus rather adapted to high frequency situations.

2.1. IS from 1 mHz to 45 kHz

A four-electrode device is used for the lower frequency range from 1 mHz to 45 kHz (Fig. 2). Its main advantage compared to a two-electrode setup is the separation of current and voltage input/output. Thereby, it avoids electrode transfer or contact impedance effects. Our custom made measurement cell (Fig. 2) consists of two acrylic reservoirs. Technical data of a first prototype version of this cell are documented in Fehr (2007). In the recent layout, the current electrodes are implemented as carbon fiber meshes and located at the outer end of these reservoirs. Notches for the sample are located at the inner end. Voltage electrodes are implemented as silver plated ring-shaped wires around these notches. The distance between current and voltage electrodes is $d_{cv} = 0.0855$ m. Neglecting the thickness of voltage electrode wires, the distance between the voltage electrodes equals the sample length $d_{vv} = 0.03$ m to $d_{vv} = 0.0566$ m, depending on the sample (Section 2.3). Thus, the distance between current electrodes is in the range of $d_{cc} = 2 \cdot d_{cv} + d_{vv} = 0.2010$ m to $d_{cc} = 0.2276$ m. For the measurement the reservoirs are filled with electrolyte solution of the same chemical composition as the pore fluid of the sample under test. Thus, we avoid perturbations of our measurement due to an exchange of the pore fluid during measurement and make sure to have homogeneous current distributions within the sample. The latter is important for any valid conversion of dielectric quantities from their macroscopic representations (cf. Section 3.1). Fluid samples are encased in plastic tubes, whereas solid samples are wrapped in cling film or bicycle inner tubes if additional stability is required. The necessary electronic measurement device is the ZEL-SIP-04 system (e.g. Zimmermann et al., 2008; Zimmermann, 2010), built at Forschungszentrum Jülich GmbH,[1] including a PC-based measurement control system, function generator (Agilent 33220A) and measurement amplifier. With the described specifications, it is possible to obtain phase data with an accuracy of about 0.1 mrad, which is the maximum instrument accuracy

---

[1] Forschungszentrum Jülich GmbH, 52425 Jülich, Germany.

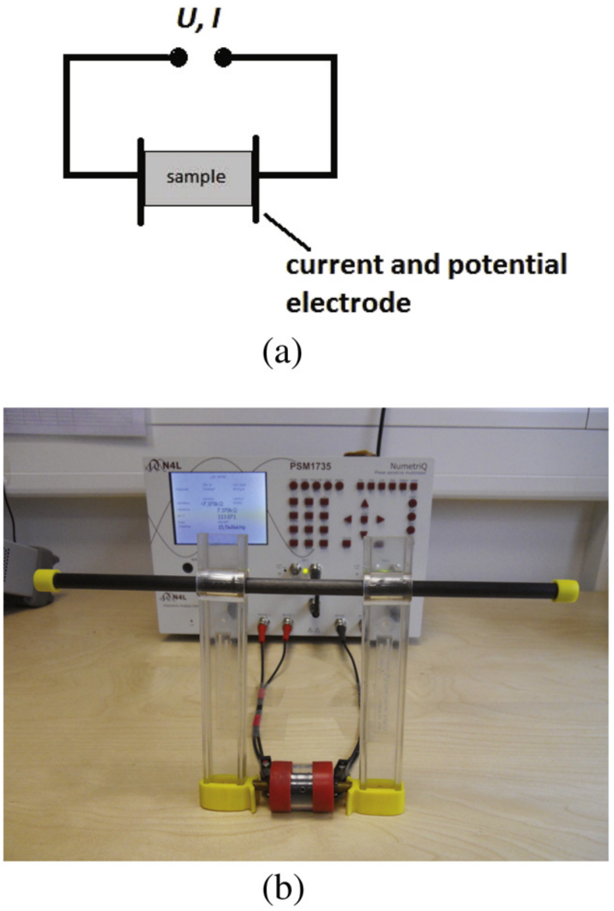

Fig. 3. (a): Principle design of the used two-electrode cell; (b): PSM1735 frequency response analyzer with Impedance Analysis Interface (IAI). The sample is installed between metal electrodes, held in a fixed position with a clamp.

specified by the manufacturer. By default, we confirmed data quality by repeated measurements of water samples with well known conductivity dispersion. The main disadvantage of the measurement technique is the increase of electromagnetic coupling between different parts of the setup for higher frequencies (cf. Section 3, Fig. 5, blue circles). Thus, we use a two-electrode setup for the higher frequencies, described in the following section.

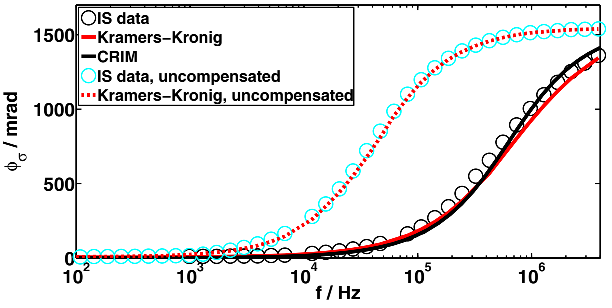

Fig. 4. Frequency dependent phase shift of a porous borosilicate sample measured by a two-electrode setup, illustrating the effect of internal instrument compensation of the two-electrode instrument. Uncompensated (cyan circles) and compensated (black circles) data of the same sample at similar fluid conductivity σ_{fluid}, temperature T and water filled porosity ϕ_{wf}. The respective Kramer–Kronig data (dashed and solid red line, Eq. (33)) confirm measurement quality in both cases. CRIM simulation (black line, Eq. (34)) suggests to prefer compensated measurements. Cf. Table 1.

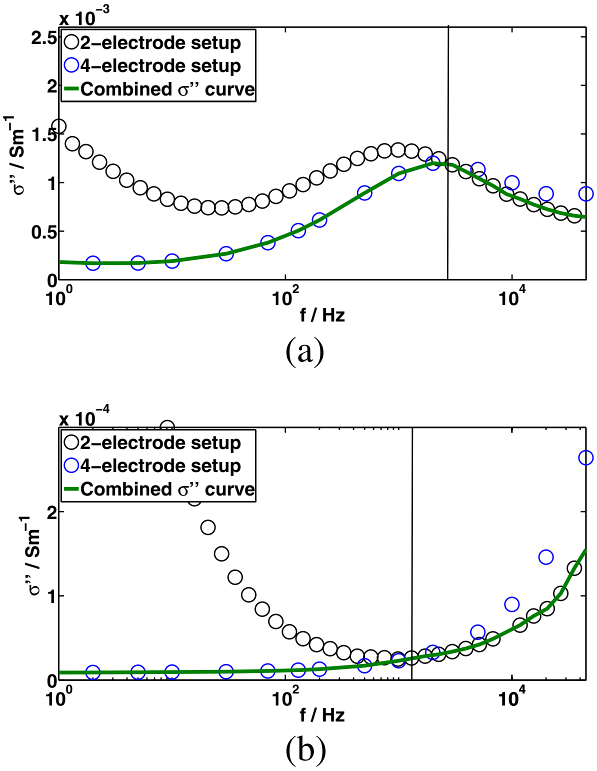

Fig. 5. Imaginary conductivity of two different samples: (a) concrete sample with strong dispersion and (b) reservoir rock sample with weak dispersion. Four-electrode data are shown as blue circles and two-electrode data as black circles, cf. Table 1. The combined data are shown as green solid line. The intercept frequency ω_{gr} (indicated by the black vertical line) was used to combine the data. For $f_{gr} = \omega_{gr}/(2\pi)$ we find values of (a) $f_{gr} = 2.7$ kHz and (b) $f_{gr} = 1.3$ kHz.

2.2. IS from 1 Hz to 10 MHz

Due to data inaccuracy of our four-electrode system at higher frequencies, we use a standard two-electrode apparatus for the higher frequency range (1 Hz to 10 MHz). It consists of a PSM1735 frequency response analyzer with Impedance Analysis Interface (IAI), both manufactured by Newtons4th Ltd (N4L). The instrument is capable of an internal compensation of stray impedance effects. Parallel and serial stray components are quantified by a classical short/open zero measurement to remove inductive/capacitive effects of leads and connections. Its advantages are shown for a porous sintered glass sample (cf. Volkmann et al., 2013), allowing measurements up to several MHz (Fig. 4).

We used this setup with two different types of electrodes: Stainless steel electrodes and brazen (CuZn39Pb3, Fig. 3) electrodes. To reduce additional impedance at the sample/electrode interface, which strongly depends on electrode/sample connection, we developed a bendable electrode mounting. Thereby, the electrode could adapt to inclined sample surfaces. Additionally, microscopic sample surface roughness and possible remaining air gaps were evened out with saturated filter paper between sample and electrode to further improve the sample/electrode contact.

We ensured calibration and data quality by standardized premeasurement tests with ohmic resistances. Additionally, we measured water samples of different salinity with satisfactory results. We obtain results in good agreement with CRIM for samples without high frequency sample polarization (Fig. 4). Nevertheless, the main disadvantage of the device, i.e. the existence of contact/transfer impedance effects in the lower part of its frequency range, remains present (cf. Section 3, Fig. 5, black circles). Thus, we use four electrode data here (Section 2.1).

2.3. Samples

We tested the proposed procedures for brine samples, porous borosilicate samples, concrete samples and reservoir rock samples to show a wide range of applicability. For the brine samples, we used demineralized water with a conductivity of about $\sigma_{fluid} \approx 1 \cdot 10^{-4}\,\mathrm{Sm}^{-1}$ and added NaCl to prepare brine samples of the desired conductivity. In particular, we prepared brine samples with an intended conductivity difference between the samples, which we measured with the four-electrode ($\sigma_{w1} \approx 2.975 \cdot 10^{-4}\,\mathrm{Sm}^{-1}$) and two-electrode ($\sigma_{w2} \approx 9.2 \cdot 10^{-4}\,\mathrm{Sm}^{-1}$) setups. Thereby, we could mimic typical conductivity deviations due to sample handling, temperature drift or accuracy between the different instruments, which are described in Sections 2.1 and 2.2. The samples were measured in a cylindrical plastic tube with a length of 0.053 m and inner diameter of 0.026 m.

Secondly, we used porous borosilicate samples as an experimental reference system (cf. Volkmann et al., 2013). These are sintered porous ceramics, manufactured by ROBU Sintered Glassfilters GmbH.[2] They consist of pure borosilicate 3.3 standard glass according to ISO 4793 and DIN/ISO 3585. The main advantage is their well-known chemical composition and narrow pore size distribution, as well as the available material characterization by the manufacturer. We used samples with pore diameters between 0.9 μm and 160 μm. The cylindrical samples had a length of 0.03 m and diameter of 0.02.

Third, we show a set of concrete samples, measured by Reichling (2013) with the procedures proposed in this paper. The concrete sample shown here had a length of 0.0407 m and diameter of 0.0296 m.

Finally, we used a set of reservoir rocks to show applicability in a geophysical context. They had diameters of 0.0298 m and lengths varying between 0.0466 m and 0.0566 m.

All solid samples have been wrapped in cling film or bicycle inner tubes (if additional stability was required) to seal the sample during measurement.

3. Data processing

There is a large variety of possible representations of a single AC dielectric quantity, i.e. the response to an electric field or its time derivative or both. Though research on a founded distinction and choice of a meaningful variable is available, e.g. by Cao and Gerhardt (1990) or Gerhardt (1994), making this choice still seems to be a quite challenging task for most researchers. Due to the importance of this question for our data processing procedure and to understand the decisive difference of the proposed method to other approaches, we give an overview over this very basic topic in Section 3.1. We summarize all possible representations of an AC dielectric quantity in Table 2 and deduce corresponding processing procedures for combining IS data of two different setups for three selected variants. In Section 3.2, we present our suggested procedure which is based on a Cartesian conductivity formulation. We discuss two popular alternative representations, the Cartesian form of impedance and the polar form of conductivity, in Sections 3.3 and 3.4, together with the corresponding processing schemes. The alternative data combination approaches as well as the suggested processing are applied to measured data in Section 5.

3.1. Choice of dielectric variables

Low frequency dielectric measurements are usually conducted with sinusoidal current/voltage signals. For such time harmonic current densities $\mathbf{j} = |\mathbf{j}|e^{i(\omega t+\phi_j)}$ and electric fields $\mathbf{E} = |\mathbf{E}|e^{i(\omega t+\phi_E)}$ — with angular frequency ω, time t and phase shift $\phi_{j,E}$ — an AC variant of Ohm's law follows from Maxwell's equation (Maxwell, 1873) for the magnetic field H:

Table 1
Symbols in the figures.

Data set	Symbol
Four-electrode data	Blue circles
Two-electrode raw data, uncompensated	Cyan circles
Two-electrode raw data, compensated	Black circles
Two-electrode corrected data	Green circles (Fig. 9: triangles, squares)
CRIM simulation (solid samples), calc. dispersion (brine)	Solid lines, color according to IS data set
Kramers–Kronig relations	Red solid, dashed or dashed & dotted lines

$$\mathbf{j} = \nabla \times \mathbf{H} \tag{1}$$

$$= \sigma\mathbf{E} + \varepsilon\,\dot{\mathbf{E}} \tag{2}$$

$$= \sigma\mathbf{E} + i\omega\varepsilon\mathbf{E} \tag{3}$$

$$= (\sigma + i\omega\varepsilon)\mathbf{E} \tag{4}$$

$$= \sigma^*\mathbf{E} \tag{5}$$

with complex conductivity

$$\sigma^* = \sigma + i\omega\varepsilon, \tag{6}$$

often rewritten as

$$\sigma^* = \sigma' + i\sigma'' \tag{7}$$

or alternatively as

$$\sigma^* = |\sigma^*|e^{i\phi_\sigma}, \tag{8}$$

where σ denotes conductivity, ε denotes permittivity, complex quantities are indicated by an asterisk, real parts by a prime and imaginary parts by double prime, phase shifts of any quantity X^* are denoted by ϕ_X. Thus, the fundamental — in terms of Maxwell's laws — representation σ^* of a dielectric quantity according to Eq. (5) already offers three ways to split into two independent variables, namely according to Eqs. (6), (7) and (8).

Some authors prefer inverse representations of the dielectric quantity. The basic one is the resistivity $\rho^* = \sigma^{*-1}$. The misconception, that ρ^* and σ^* are essentially the same, can lead to numerous errors, e.g. when raw data averaging and forming the inverse are performed in reverse order.

Another common dielectric representation emphasizes the dielectric components which are proportional to the time derivative of electric fields instead of the electric fields themselves. Therefore, Eq. (2) is rephrased differently:

$$\mathbf{j} = \frac{\sigma}{i\omega}\dot{\mathbf{E}} + \varepsilon\,\dot{\mathbf{E}} \tag{9}$$

$$= \left(\frac{\sigma}{i\omega} + \varepsilon\right)\dot{\mathbf{E}} \tag{10}$$

$$= \varepsilon^*\dot{\mathbf{E}} \tag{11}$$

with complex permittivity $\varepsilon^* = [i\omega]^{-1} \cdot \sigma^*$. The popularity of this representation strongly increases with frequency.

Another important set of representations are the macroscopic and non-normalized variants of the dielectric quantity. If the microscopic

---

[2] ROBU Sintered Glassfilters GmbH, Schützenstraße 13, D-57644 Hattert, Germany.

Table 2
Numerous possible representations of the same dielectric variable as two real valued quantities $a(\omega)$ and $b(\omega)$.

Representation	Relation	Form	$a(\omega)$	$b(\omega)$	No.
Conductivity	$\sigma^* = \sigma^*$	$\begin{cases} = a + ib \\ = \lvert a\rvert \cdot exp(ib) \end{cases}$	σ' $\sqrt{\sigma'^2 + \sigma''^2}$	σ'' $arctan\left(\frac{\sigma''}{\sigma'}\right)$	1 2
Resistivity	$\rho^* = \sigma^{*\,-1}$	$\begin{cases} = a + ib \\ = \lvert a\rvert \cdot exp(ib) \end{cases}$	$(\sigma'^2 + \sigma''^2)^{-1}\sigma'$ $\left[\sqrt{\sigma'^2 + \sigma''^2}\right]^{-1}$	$-(\sigma'^2 + \sigma''^2)^{-1}\sigma''$ $-arctan\left(\frac{\sigma''}{\sigma'}\right)$	3 4
Admittance	$Y^* = G \cdot \sigma^*$	$\begin{cases} = a + ib \\ = \lvert a\rvert \cdot exp(ib) \end{cases}$	$G \cdot \sigma'$ $G \cdot \sqrt{\sigma'^2 + \sigma''^2}$	$G \cdot \sigma''$ $arctan\left(\frac{\sigma''}{\sigma'}\right)$	5 6
Impedance	$Z^* = [G \cdot \sigma^*]^{-1}$	$\begin{cases} = a + ib \\ = \lvert a\rvert \cdot exp(ib) \end{cases}$	$[G \cdot (\sigma'^2 + \sigma''^2)]^{-1}\sigma'$ $\left[G \cdot \sqrt{\sigma'^2 + \sigma''^2}\right]^{-1}$	$-[G \cdot (\sigma'^2 + \sigma''^2)]^{-1}\sigma''$ $-arctan\left(\frac{\sigma''}{\sigma'}\right)$	7 8
Permittivity	$\varepsilon^* = [i\omega]^{-1} \cdot \sigma^*$	$\begin{cases} = a + ib \\ = \lvert a\rvert \cdot exp(ib) \end{cases}$	$\omega^{-1}\sigma''$ $\omega^{-1}\sqrt{\sigma'^2 + \sigma''^2}$	$-\omega^{-1}\sigma'$ $arctan\left(\frac{\sigma''}{\sigma'}\right) - \frac{\pi}{2}$	9 10
Permittivity^{-1}	$\varepsilon^{*\,-1} = i\omega \cdot \sigma^{*\,-1}$	$\begin{cases} = a + ib \\ = \lvert a\rvert \cdot exp(ib) \end{cases}$	$\omega(\sigma'^2 + \sigma''^2)^{-1}\sigma''$ $\omega\left[\sqrt{\sigma'^2 + \sigma''^2}\right]^{-1}$	$\omega(\sigma'^2 + \sigma''^2)^{-1}\sigma'$ $-arctan\left(\frac{\sigma''}{\sigma'}\right) + \frac{\pi}{2}$	11 12
Permittivity$_{\text{non-norm}}$	$E^* = [i\omega]^{-1}G \cdot \sigma^*$	$\begin{cases} = a + ib \\ = \lvert a\rvert \cdot exp(ib) \end{cases}$	$\omega^{-1}G \cdot \sigma''$ $\omega^{-1}G\sqrt{\sigma'^2 + \sigma''^2}$	$-\omega^{-1}G \cdot \sigma'$ $arctan\left(\frac{\sigma''}{\sigma'}\right) - \frac{\pi}{2}$	13 14
Permittivity$^{-1}_{\text{non-norm}}$	$E^{*\,-1} = i\omega \cdot [G \cdot \sigma^*]^{-1}$	$\begin{cases} = a + ib \\ = \lvert a\rvert \cdot exp(ib) \end{cases}$	$\omega[G \cdot (\sigma'^2 + \sigma''^2)]^{-1}\sigma''$ $\omega\left[G \cdot \sqrt{\sigma'^2 + \sigma''^2}\right]^{-1}$	$\omega[G \cdot (\sigma'^2 + \sigma''^2)]^{-1}\sigma'$ $-arctan\left(\frac{\sigma''}{\sigma'}\right) + \frac{\pi}{2}$	15 16
Classic	$[\sigma = \sigma', \varepsilon = \omega^{-1}\sigma'']$	$\{= a + i\omega \cdot b$	σ'	$\omega^{-1}\sigma''$	17

quantities are spatially homogeneous for a sample of length l and cross-section area A, voltage $\mathbf{U}$ and current $\mathbf{I}$ are related by:

$$\mathbf{U} = l \cdot \mathbf{E} \tag{12}$$

$$= l\rho^* \cdot \mathbf{j} \tag{13}$$

$$= \frac{l\rho^*}{A} \cdot \mathbf{I} \tag{14}$$

$$= Z^* \cdot \mathbf{I} \tag{15}$$

with impedance

$$Z^* = \frac{l}{A} \cdot \rho^* \tag{16}$$

$$= G^{-1} \cdot \rho^*, \tag{17}$$

G being a geometry factor. Thus, the impedance Z^* is the non-normalized macroscopic variant of the resistivity ρ^*.

The above mentioned operations, e.g. calculating an inverse or preferring macroscopic variants, can be combined freely to make more variables possible. In Table 2 we summarize all resulting representations and how they split into real valued dispersion curves $a(\omega)$ and $b(\omega)$, e.g. into the real part $a(\omega) = \sigma'(\omega)$ of conductivity and imaginary part $b(\omega) = \sigma''(\omega)$ of conductivity. After the description of the suggested choice of variables and derivation of the resulting processing procedures in Section 3.2, we give counterexamples of popular suboptimal choices of variables and corresponding calculations in Sections 3.3 and 3.4.

3.2. Suggested processing procedure

We propose a procedure for a combination of two individual dielectric data sets, based on a Cartesian conductivity formulation $\sigma^* = \sigma' + i\sigma''$ (Table 2, first row). This choice implies, we consider the variables σ' and σ'' as independently error affected variables.

As a precondition, we need to fulfill the experimental requirement that the dispersive effects inherent to each setup, e.g. electromagnetic coupling and/or transfer impedances, are both decayed at some mutual point within an overlapping frequency range (between 1 Hz and 45 kHz). This precondition is the decisive criterion for the choice of hardware and development of lab procedures for the two necessary impedance experiments (Sections 2.1 and 2.2). The requirement is met, if a mutual confirmation of imaginary conductivity can be achieved for a certain (intermediate/overlapping) frequency range. If at least an intercept frequency ω_{gr} with $\sigma''_{4p}(\omega_{gr}) = \sigma''_{2p}(\omega_{gr})$ exists, we assume to find the best approximation for the abovementioned undisturbed state at this frequency ω_{gr} (Fig. 5). Subsequent correction attempts might be applied, if the requirement cannot be met experimentally (e.g. Kavian, 2011). We only consider the former case, where such subsequent data manipulation is not necessary.

Under the above precondition, we propose a correction procedure for remaining non-dispersive effects in real conductivity $\sigma'(\omega)$. These effects may arise not only from an additional non-dispersive transfer impedance contribution, but as well from any kind of time dependent disturbance, e.g. temperature differences, when the sample is assembled in the other experimental setup or simply from differences in accuracy between the two setups. Thus, we can overcome the assumption of perfect match between data sets from different subsequent experiments (e.g. Lockner and Byerlee, 1985).

From IS measurements on water, we find that the four-electrode setup provides the more accurate real part and absolute value data (cf. Figs. 7 and 8). Thus, we propose to correct the two-electrode measurement by means of the four-electrode measurement for this type of error.

This leads us to a rather simple processing procedure for the complex conductivity $\sigma^*_{4p/2p}$, real parts $\sigma'_{4p/2p}$ and imaginary parts $\sigma''_{4p/2p}$: First, we eliminate electrode polarization and coupling effects by a switch from four-electrode to two-electrode data at the intercept ω_{gr} between the $\sigma''(\omega)$ curves (Fig. 5).

At this frequency ω_{gr} with $\sigma''_{4p}(\omega_{gr}) = \sigma''_{2p}(\omega_{gr})$, we are able to correct the disturbed complex two-electrode datum by

$$\sigma^*_{2p}\left(\omega_{gr}\right) = \sigma'_{2p}\left(\omega_{gr}\right) + i \cdot \sigma''_{2p}\left(\omega_{gr}\right) \tag{18}$$

$$= \sigma'_{2p}\left(\omega_{gr}\right) + i \cdot \sigma''_{4p}\left(\omega_{gr}\right) \tag{19}$$

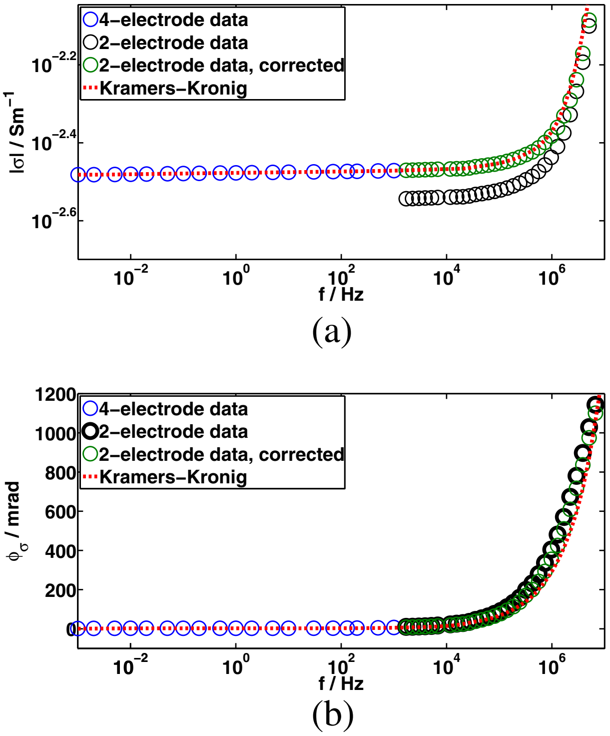

Fig. 6. Bode plot of a reservoir core sample. Four-electrode (blue circles), raw two-electrode data (black circles) and processed two-electrode data (green circles, Eq. (24)). Combined wideband data are compatible with Kramers–Kronig relations (dashed red line), cf. Table 1.

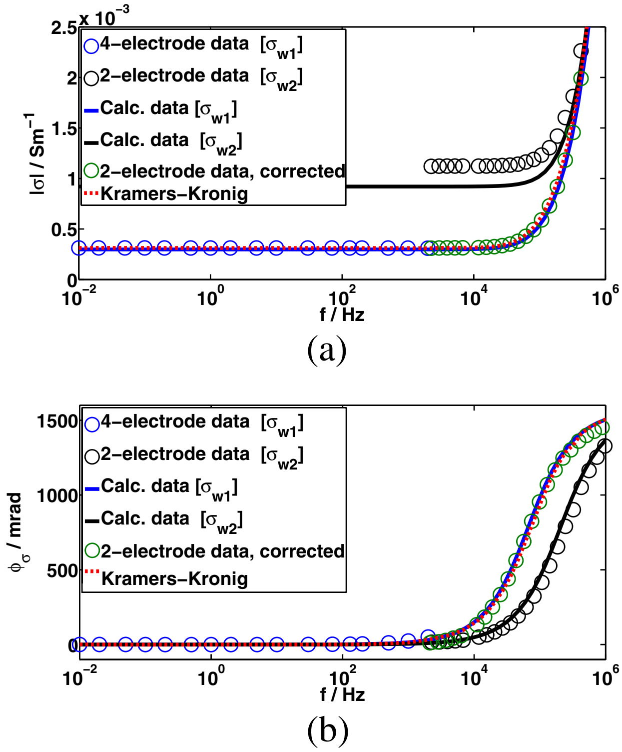

Fig. 7. Bode plot of water samples. Four-electrode data at $\sigma_{w1} = (2.975 \pm 0.5852) \cdot 10^{-4}$ Sm^{-1} (blue circles) and simulated dispersion (blue line). Two-electrode data of intentionally conductivity altered water at $\sigma_{w2} \approx 9.2 \cdot 10^{-4}$ Sm^{-1} (black circles) and simulated dispersion (black line). Corrected two-electrode data (green circles) and Kramers–Kronig relations for the combined data set (dashed red line), cf. Table 1.

$$= \sigma'_{2p}\left(\omega_{gr}\right) + \left[\sigma^*_{4p}\left(\omega_{gr}\right) - \sigma'_{4p}\left(\omega_{gr}\right)\right] \tag{20}$$

$$= \sigma^*_{4p}\left(\omega_{gr}\right) + \left[\sigma'_{2p}\left(\omega_{gr}\right) - \sigma'_{4p}\left(\omega_{gr}\right)\right] \tag{21}$$

$$= \sigma^*_{4p}\left(\omega_{gr}\right) + \Delta\sigma' \tag{22}$$

with

$$\Delta\sigma' = \left[\sigma'_{2p}\left(\omega_{gr}\right) - \sigma'_{4p}\left(\omega_{gr}\right)\right]. \tag{23}$$

As described above, we assume data points with $\sigma''_{4p}(\omega) = \sigma''_{2p}(\omega)$ to represent the best approximation for undisturbed data in terms of frequency dependent effects, if a mutual confirmation in a range of frequencies is not achievable. Thus, the term $\Delta\sigma'$ mainly describes additional frequency independent effects. Therefore, we generalize Eq. (22) to

$$\sigma^*_{2p,true}(\omega) = \sigma^*_{2p,meas.}(\omega) - \Delta\sigma' \tag{24}$$

for frequencies $\omega \geq \omega_{gr}$. Thus, we calculate the true data $\sigma_{2p,true}^*(\omega)$ from the disturbed data $\sigma_{2p,meas.}^*(\omega)$ by an additive correction $\Delta\sigma'$ of the real part of conductivity, determined at the intercept frequency ω_{gr} of the imaginary part of conductivity. This correction is a direct consequence of the choice of dielectric variables from Table 2. For comparison and to emphasize the non-trivial character of this processing step, we discuss two different approaches in the following sections. Results are introduced in Section 5, including a comparison to the alternative approaches in Section 5.2.

3.3. Alternative approach 1

As a first alternative approach, we consider the impedance in Cartesian form (Table 2, representation 7) to be the appropriate dielectric representation. We thereby assume Z' and Z'' to be independently error affected quantities. In analogy to the correction approach for the Cartesian conductivity formulation, we assume the minimal dispersive error at the intercept frequency ω_{gr} of imaginary impedances of the two-electrode and the four-electrode measurements, i.e. $Z''_{4p}\left(\omega_{gr}\right) = Z''_{2p}\left(\omega_{gr}\right)$. A correction procedure for non-dispersive disturbances follows analogous to the derivation of Eq. (24):

$$Z^*_{2p,true}(\omega) = Z^*_{2p,meas.}(\omega) - \Delta Z', \tag{25}$$

with

$$\Delta Z' = \left[Z'_{2p}\left(\omega_{gr}\right) - Z'_{4p}\left(\omega_{gr}\right)\right]. \tag{26}$$

Alternatively, this approach can be derived from the concept of an additional disturbing resistance, which is only present in one of the measurements, e.g. the two-electrode setup. Considering it as an element of an electrical network in series connection, one would attempt to subtract this resistance according to Kirchhoff's circuit laws, thus end up at Eq. (25). Results for the described procedure are shown in Section 5.2.

3.4. Alternative approach 2

As second alternative, we consider the polar form of conductivity (Table 2, representation 2) to be the appropriate dielectric representation.

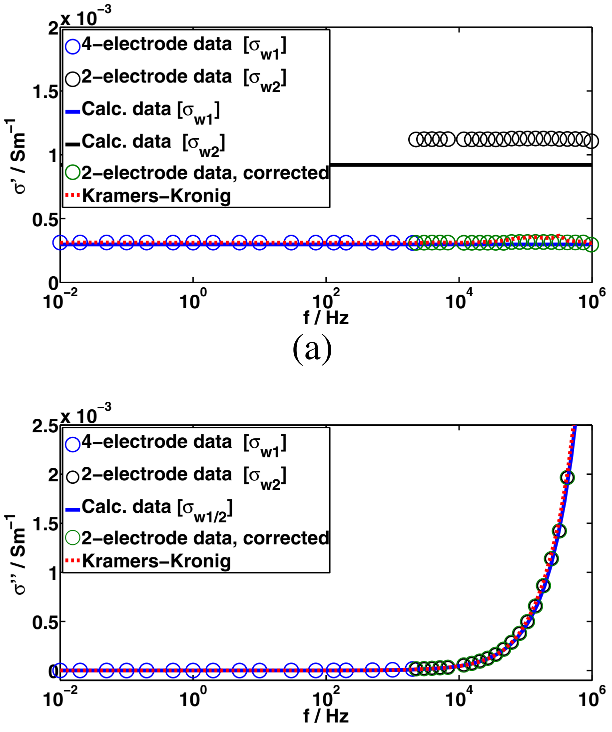

(a)

(b)

Fig. 8. Real σ' and imaginary σ'' conductivity of water samples. Four-electrode data at $\sigma_{w1} = (2.975 \pm 0.5852) \cdot 10^{-4}$ Sm^{-1} (blue circles) and simulated dispersion ((a): blue line, (b): merged with black line). Two-electrode data of intentionally conductivity altered water at $\sigma_{w2} \approx 9.2 \cdot 10^{-4}$ Sm^{-1} (black circles) and simulated dispersion (black line). Corrected two-electrode data (green circles), Kramers–Kronig relations for the combined data set (dashed red line), cf. Table 1.

We thereby assume $|\sigma|$ and φ_{σ^*} to be independently error affected quantities. If we then identify the minimal dispersive error at the frequency ω_{gr} of equally low phase shifts $\phi_{4p}(\omega_{gr}) = \phi_{2p}(\omega_{gr})$, a correction procedure for non-dispersive disturbances follows according to:

$$\sigma^*_{2p}\left(\omega_{gr}\right) = \left|\sigma^*_{2p}\left(\omega_{gr}\right)\right| e^{i\phi_{2p}\left(\omega_{gr}\right)} \qquad (27)$$

$$= \left|\sigma^*_{2p}\left(\omega_{gr}\right)\right| e^{i\phi_{4p}\left(\omega_{gr}\right)} \qquad (28)$$

$$= \frac{\left|\sigma^*_{2p}\left(\omega_{gr}\right)\right|}{\left|\sigma^*_{4p}\left(\omega_{gr}\right)\right|} \cdot \sigma^*_{4p}\left(\omega_{gr}\right) \qquad (29)$$

$$= F_{\omega_{gr}} \cdot \sigma^*_{4p}\left(\omega_{gr}\right) \qquad (30)$$

with correction factor

$$F_{\omega_{gr}} = \frac{\left|\sigma^*_{2p}\left(\omega_{gr}\right)\right|}{\left|\sigma^*_{4p}\left(\omega_{gr}\right)\right|}. \qquad (31)$$

Again neglecting remaining dispersive error fractions, one would adjust data according to:

$$\sigma^*_{2p,true}(\omega) = F^{-1}_{\omega_{gr}} \cdot \sigma^*_{2p,meas.}(\omega). \qquad (32)$$

Thus, in the typical Bode plot representation the ratio of absolute values would have evolved as a multiplicative correction factor. Results are shown in Section 5.2.

4. Validation techniques

We use a three step data quality estimation procedure. First, we check data consistency using the Kramers–Kronig relations (e.g. McKubre et al., 1987). Secondly, we predict high frequency data using the Complex Refractive Index Model (CRIM), a model for calculating high frequency complex permittivity (e.g. Cosenza et al., 2009). Thereby, we check physical integrity of our processing which, if necessary, alters high frequency data. Third, we adapt typical empirical model functions, e.g. multi-Cole–Cole, to our wideband data to show that they are fully applicable for further data analysis.

We use a set of 4 different types of samples to test the generalizability of our approach. These are brine samples, porous borosilicate samples, concrete samples and reservoir rock samples (Section 2.3).

4.1. Kramers–Kronig relations

We use the Kramers–Kronig relations (McKubre et al., 1987) to check data consistency. The Kramers–Kronig relations connect the two variables, e.g. real and imaginary part, of complex data. We calculate the imaginary part $Z''(\omega)$ of the impedance from the real part $Z'(\omega)$ of the data:

$$Z''(\omega) = -\left(\frac{2\omega}{\pi}\right) \int_0^\infty \frac{Z'(x) - Z'(\omega)}{x^2 - \omega^2} dx. \qquad (33)$$

The above relation allows to identify deviations between calculated and measured data which would e.g. imply data inconsistencies in terms of causality, linearity or stability of the system (McKubre et al., 1987). It can be applied to check data quality and validity of our correction procedure at the same time.

4.2. CRIM simulation

The Complex Refractive Index Model (CRIM) allows to simulate the dielectric quantity ε' of rocks in the high frequency limit ($\omega \to \infty$), if the volume fractions $\frac{V_i}{V_{tot}}$ and the high frequency permittivities ε_i' of the solid and fluid rock constituents are known, e.g. of rock matrix, air and additional liquid phases (water or oil). It is then given by

$$\sqrt{\varepsilon'_{CRIM}} = \sum_i \frac{V_i \sqrt{\varepsilon_i'}}{V_{tot}}, \qquad (34)$$

where the effective permittivity ε'_{CRIM} is the squared mean value of the square roots of the permittivities ε_i' of the components, weighted by their volume fractions V_i/V_{tot} (e.g. Cosenza et al., 2009). We calculate water permittivity according to the model of Klein and Swift (1977) from brine conductivity and temperature, which we measure separately. We extract low frequency conductivity σ_{lf}' from our measurement data and calculate the complex conductivity model according to

$$\sigma^*_{CRIM} = \sigma'_{\mathrm{lf}} + i\omega\varepsilon'_{CRIM}. \qquad (35)$$

The resulting spectra simulate a sample behavior without additional (e.g., Maxwell–Wagner) polarization effects. Since our processing (Eq. (24)) does not affect σ'', CRIM mainly checks the PSM1735 instrument compensation quality (Section 2.2) or indicates the presence of additional high frequency sample polarization (Section 1).

4.3. Applicability of Cole–Cole models

IS data are often described by means of empirical models for further analysis. The resulting model parameters are then related to physical properties. Adequate model functions are often of Cole–Cole type (Cole and Cole, 1941)

$$\rho(\omega) = \rho_0\left[1 - m\left(1 - \frac{1}{1 + (i\omega\tau)^c}\right)\right], \tag{36}$$

with DC — resistivity $\rho_0 = \rho(\omega = 0)$, chargeability m, frequency exponent c and time constant τ. This representation can also be expressed as electrical equivalent circuit. Though often not in a unique way, Cole–Cole models are adapted to a wide range of experimental data. Therefore, several modifications of the classical form (Eq. (36)) exist. An overview of this type of models is given e.g. in Dias (2000). However, recent research tends to introduce more generalized forms, e.g. Debye-decomposition (Nordsiek and Weller, 2008), to analyze IS data. Due to their empirical character, most of these fitting approaches lack physical meaning initially. Nevertheless, they are popular due to their descriptive power. In conductivity notation, Eq. (36) leads to (cf. e.g. Zimmermann, 2010)

$$\sigma^*(\omega) = \sigma_0\left[1 + m\left(\frac{(i\omega\tau)^c}{1 + (i\omega\tau)^c(1 - m)}\right)\right], \tag{37}$$

with $\sigma_0 = \rho_0^{-1}$.

We use the in-house Matlab code CFit,[3] for fitting complex resistivity spectra. CFit can be easily adapted to a particular frequency range or used with custom-made model functions. For our wideband data, we implemented the following wideband model function

$$\sigma^*(\omega) = \sigma^*_{CC,LF} + \sigma^*_{CC,HF} + i\varepsilon\omega, \tag{38}$$

consisting of a low frequency $\sigma_{CC,LF}$ and high frequency $\sigma_{CC,HF}$ Cole–Cole model (Eq. (37)), combined with $i\varepsilon\omega$. Thereby, we consider two different relaxation processes and (static) permittivity influences. Besides the data consistency information, which is checked by Kramers–Kronig relation (Eq. (33), cf. Esteban and Orazem, 1991), we can thereby compare fitting parameters of Cole–Cole Eq. (38), e.g. permittivity ε, to corresponding theoretical models, e.g. CRIM simulation (Eq. (34)).

In summary, we check Kramers–Kronig relations (Eq. (33)), CRIM model (Eq. (34)) and Cole–Cole applicability (Eq. (38)) for a set of reference samples (Section 2.3).

5. Application of data combination approaches and validation methods to IS data

In the following, we apply the introduced correction approaches (Section 3) to IS data of reference samples (Section 2.3). Subsequently, we validate the combined data using the methods explained in Section 4.

5.1. Water samples

In the studied frequency range, water samples show a dispersion according to Eq. (6) with $\sigma, \varepsilon = const.$. The values of σ and ε can be calculated, if salt concentration and temperature are known. This makes water an ideal reference sample. We prepared samples with an intended difference in the sample conductivities between $\sigma_{w,1} = (2.975 \pm 0.5852) \cdot 10^{-4}\ \mathrm{Sm}^{-1}$ for the four-electrode measurement and $\sigma_{w,2} \approx 9.2 \cdot 10^{-4}\ \mathrm{Sm}^{-1}$ for the two-electrode measurement. The conductivity difference shall represent a typical contamination due to sample handling or storage. Figs. 7 and 8 confirm that the four-electrode method is more accurate than the two-electrode method in terms of real or absolute valued conductivity. Imaginary components are similar (Fig. 8) for both measurements. Thus, we obtain differences in phase shift (Fig. 7) due to the offset in the real part (Fig. 8). All of these confirm our correction approach of σ' and σ'' being independently polarized quantities with σ'' incorporating dispersive, σ' incorporating non-dispersive errors. Our processing procedure leads to data sets in agreement to simulated data of the original low conductive brine while data stay compatible with Kramers–Kronig relations (Figs. 7 and 8).

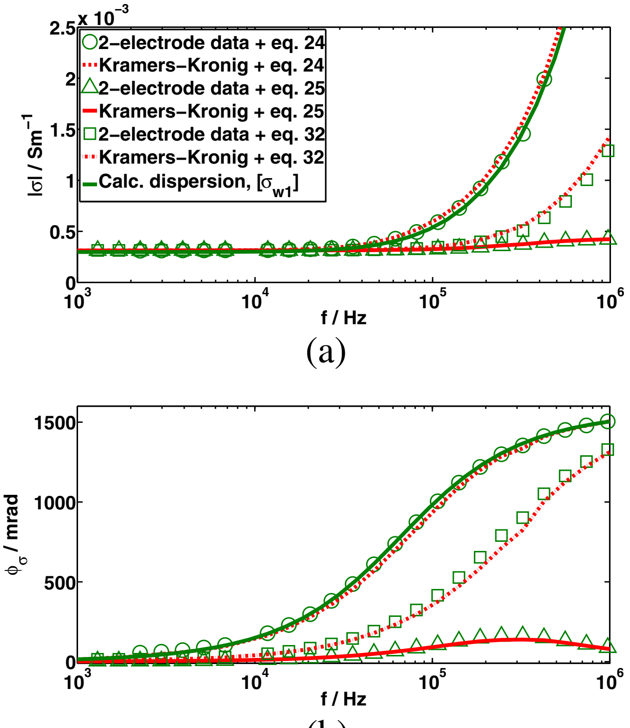

(a)

(b)

Fig. 9. Bode plot of the same water sample as in Figs. 7 and 8, processed according to Eq. (24) (green circles), according to Eq. (25) (green triangles) and according to Eq. (32) (green squares) with corresponding Kramers–Kronig data (red dashed/dotted/solid lines), cf. Table 1. The theoretical brine dispersion ($\sigma_{w1} = (2.975 \pm 0.5852) \cdot 10^{-4}\ \mathrm{Sm}^{-1}$) is shown as a green line. All calculations are in agreement with Kramers–Kronig relations, but only Eq. (24) provides physically meaningful results.

5.2. Comparison of data combination approaches

In Fig. 9, we compare the results of the suggested procedures (Eq. (24)) with alternative correction approaches given by Eqs. (25) and (32) for the same brine samples as used in Figs. 7 and 8. The Cartesian impedance calculation (Eq. (25)) and the polar conductivity calculation (Eq. (32)) both agree well in terms of Kramers–Kronig transforms, indicating consistent raw data and correct derivation of Eqs. (25) and (32). This applies to our suggested correction (Eq. (24)) as well, but only these Cartesian conductivity data are in agreement with the simulated dispersion of the brine sample. Thus, in our context $\sigma'(\omega)$ and $\sigma''(\omega)$, but neither the pair $Z'(\omega)$ and $Z''(\omega)$ nor the pair $|\sigma|(\omega)$ and $\phi_{\sigma^*}(\omega)$ appears as independently affected quantities.

To illustrate the difference between the combined curves in Fig. 9, we translate the results of the alternative approaches 1 (Section 3.3) and 2 (Section 3.4) into the suggested Cartesian conductivity formulation (Section 3.2). Therefore, we rephrase the respective equations.

First, the Cartesian impedance approach (green triangles in Fig. 9, Section 3.3) is reproduced in Cartesian conductivity formulation. As

---

[3] By Helge Trautmann, Norbert Klitzsch and Alexander Schmidt, Applied Geophysics and Geothermal Energy, E.ON ERC, RWTH Aachen University, (personal communication).

described in Section 3.3, we first identify the intercept frequency (or frequency range) $\omega = \omega_{gr}$ of equally low imaginary impedance:

$$Z''_{4p}\left(\omega_{gr}\right) = Z''_{2p}\left(\omega_{gr}\right). \tag{39}$$

This condition is translated into Cartesian conductivity representation, using Table 2:

$$\frac{\sigma''_{4p}\left(\omega_{gr}\right)}{\sigma'^{2}_{4p}\left(\omega_{gr}\right) + \sigma''^{2}_{4p}\left(\omega_{gr}\right)} = \frac{\sigma''_{2p}\left(\omega_{gr}\right)}{\sigma'^{2}_{2p}\left(\omega_{gr}\right) + \sigma''^{2}_{2p}\left(\omega_{gr}\right)}. \tag{40}$$

For $\omega \geq \omega_{gr}$, the two electrode data are corrected according to Eq. (25):

$$Z^{*}_{2p,true}(\omega) = Z^{*}_{2p,meas.}(\omega) - \Delta Z', \tag{41}$$

with

$$\Delta Z' = \left[Z_{2p}{}'\left(\omega_{gr}\right) - Z_{4p}{}'\left(\omega_{gr}\right)\right]. \tag{42}$$

In Cartesian conductivity representation, this is expressed as:

$$\sigma^{*}_{2p,true}(\omega) = \frac{1}{A_{\omega_{gr}}} \cdot \left[\frac{1}{1 - A_{\omega_{gr}} \sigma^{*}_{2p,meas.}(\omega)} - 1\right] \tag{43}$$

with

$$A_{\omega_{gr}} = G \cdot \Delta Z' \tag{44}$$

$$= \frac{\sigma'_{2p}\left(\omega_{gr}\right)}{\left(\sigma'^{2}_{2p}\left(\omega_{gr}\right) + \sigma''^{2}_{2p}\left(\omega_{gr}\right)\right)} - \frac{\sigma'_{4p}\left(\omega_{gr}\right)}{\left(\sigma'^{2}_{4p}\left(\omega_{gr}\right) + \sigma''^{2}_{4p}\left(\omega_{gr}\right)\right)}. \tag{45}$$

Secondly, we reproduce the polar conductivity approach (green squares in Fig. 9, Section 3.4) in Cartesian conductivity representation. Since both representations are conductivity approaches, the form of Eq. (32) is conserved, but still the change of variables complicates the calculations. According to Section 3.4, we identify the intercept frequency (or frequency range) $\omega = \omega_{gr}$ of equal phase shifts:

$$\phi_{4p}\left(\omega_{gr}\right) = \phi_{2p}\left(\omega_{gr}\right). \tag{46}$$

In Cartesian conductivity representation, this condition means:

$$arctan\left(\frac{\sigma''_{4p}}{\sigma'_{4p}}\right) = arctan\left(\frac{\sigma''_{2p}}{\sigma'_{2p}}\right). \tag{47}$$

For $\omega \geq \omega_{gr}$, the two electrode data are corrected according to Eq. (32):

$$\sigma^{*}_{2p,true}(\omega) = F^{-1}_{\omega_{gr}} \cdot \sigma^{*}_{2p,meas.}(\omega), \tag{48}$$

where F is calculated in Cartesian representation by:

$$F_{\omega_{gr}} = \sqrt{\frac{\sigma'^{2}_{2p}\left(\omega_{gr}\right) + \sigma''^{2}_{2p}\left(\omega_{gr}\right)}{\sigma'^{2}_{4p}\left(\omega_{gr}\right) + \sigma''^{2}_{4p}\left(\omega_{gr}\right)}}. \tag{49}$$

Thus, the alternative approaches lead to more complex and non-intuitive procedures in the suggested Cartesian conductivity representation. According to Eqs. (43) and (48), these affect both $\sigma'(\omega)$ and $\sigma''(\omega)$.

5.3. Reservoir rock samples

An example of processed reservoir rock data is shown in Fig. 6. The sandstone sample was saturated with an NaCl solution of conductivity $\sigma_f \approx 2 \cdot 10^{-1}$ Sm^{-1}. A set of 22 reservoir samples was processed with similar results.

5.4. Porous borosilicate samples

We studied porous borosilicate samples extensively. A typical data set is shown in Fig. 10. Processed four-electrode (blue circles) and two-electrode (green circles) data are already combined for this example. Additionally, Kramers–Kronig data (dashed red line) and CRIM data (blue line) are depicted. Kramers–Kronig relations indicate a consistent measurement and processing routine. CRIM data agree well in the high frequency range, whereas for intermediate frequencies additional polarization occurs and thus data deviate from the CRIM simulation. Applicability for further analysis was confirmed using Cole–Cole type models. Therefore, the rock permittivity ε obtained from Eq. (38) is compared with ε_{CRIM} calculated according to Eq. (34) (Fig. 11). It provides a good indicator for the quality of instrument stray impedance compensation (cf. Fig. 4) and/or additional high frequency polarization, which is not covered by CRIM. Applicability of Cole–Cole Eq. (38) for low and intermediate frequencies of the combined data sets was extensively studied for the borosilicate sample type in Volkmann et al. (2013), e.g. showing reasonable low

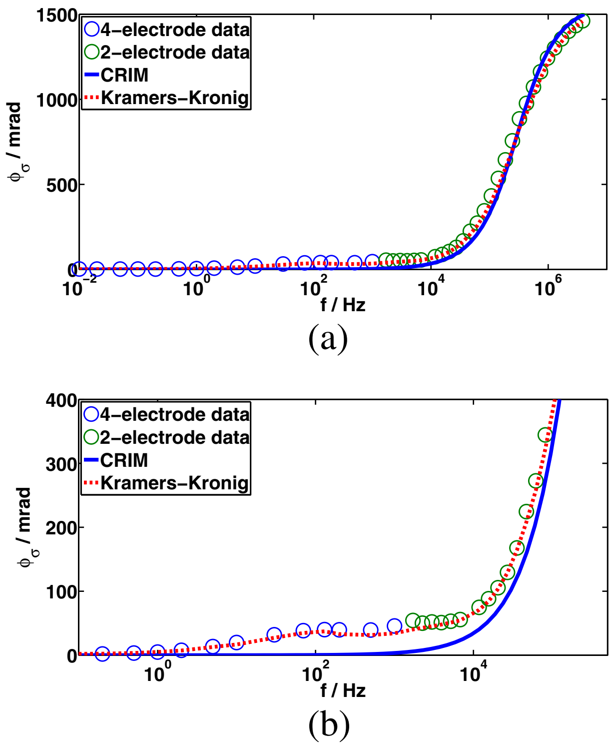

Fig. 10. Phase shift data of a sintered porous borosilicate sample (nominal pore size $d_{por} = 1.0\ \mu m - 1.6\ \mu m$, fluid conductivity $\sigma_f \approx 3.3 \cdot 10^{-4}$ Sm^{-1}). Four-electrode data (blue circles), processed two-electrode data (green circles), CRIM simulation (blue line) and Kramers–Kronig relations (dashed red line), cf. Table 1. Agreement with Kramers–Kronig relations and deviations from CRIM simulation at intermediate frequencies indicate the presence of polarization effects.

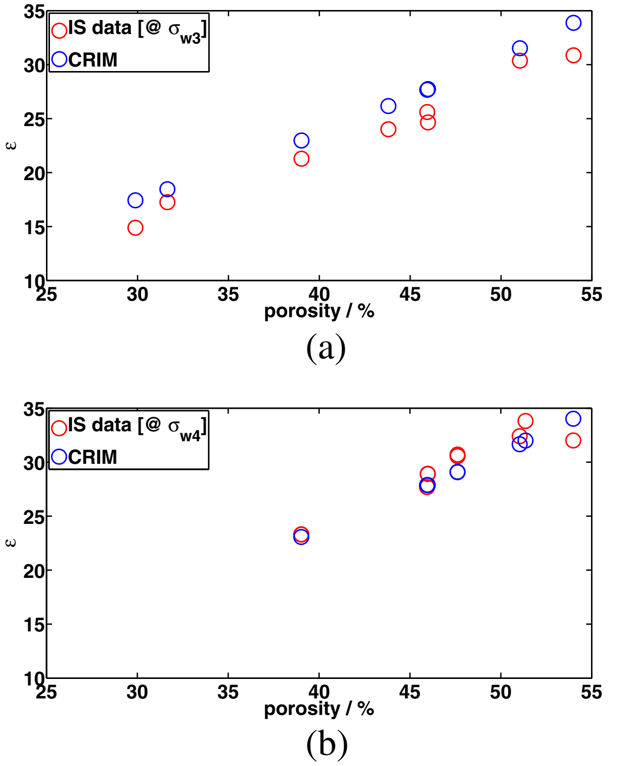

(a)

(b)

Fig. 11. Permittivity ε from IS data (red circles) and CRIM simulation (+Klein–Swift, blue circles) for borosilicate samples. Mean values of fluid conductivity: (a) $\sigma_{w3} \approx 5 \cdot 10^{-2}$ Sm^{-1} at $T \approx 20$ °C and (b) $\sigma_{w4} \approx 3 \cdot 10^{-3}$ Sm^{-1} at $T \approx 20$ °C. For the calculations, accurate conductivity values have been used at each data point. In (a), permittivity from IS is systematically too low (possibly due to inaccurate instrument compensation, Section 2.2), whereas data in (b) are more accurate and possibly subject to additional polarization effects.

frequency Cole–Cole time constant extracted from the combined wideband data.

5.5. Concrete samples

The set of concrete samples measured by Reichling (2013) shows applicability for sample types with very strong inherent sample dispersion at the point of lowest dispersive error $\omega = \omega_{gr}$ (Fig. 5). Fig. 12 shows the complete Bode plot for this exemplary data set after processing. Kramers–Kronig relations (Fig. 12, dashed red line) come to their validity limit for data quality estimation, if the measurement data do not reach their DC limit within the studied frequency range (e.g. Esteban and Orazem, 1991, and references therein). Thus, the high phase shifts at lowest frequencies, present for several samples of this study, are responsible for deviations between measured and Kramers–Kronig transformed data here. We have to dispense CRIM, because necessary porosity and dry sample permittivity values are not available. Thus, the processing scheme could be applied, but not be validated here. For further results and conclusions, we refer to the detailed analysis in Reichling (2013).

5.6. Validity limit of the suggested procedure

To show the limits of our procedure, raw imaginary conductivity data of a rock sample with high fluid salinity of $\sigma_f \approx 22.2$ Sm^{-1} at $T = 20.6$ °C were taken as well (Fig. 13). Here, the dispersive error of the two-electrode measurement remains irreducibly high within the frequency overlap of the two instruments due to electrode/contact impedance effects. According to Section 3.2, a frequency range of mutual confirmation of imaginary conductivity between the setups is necessary, if Eq. (24) is expected to give an exact correction. We apply it as well to data which have at least a frequency ω_{gr} of equally small imaginary conductivity. Then Eq. (24) serves as an approximate solution, which we must validate according to Section 4. For high fluid salinity, such a frequency ω_{gr} does not exist. Thus, e.g. for high saturating fluid conductivity, the proposed method is not applicable. The same applies for any other case, where imaginary conductivity is influenced by dispersive errors in the entire overlapping frequency range of both setups (cf. Section 3).

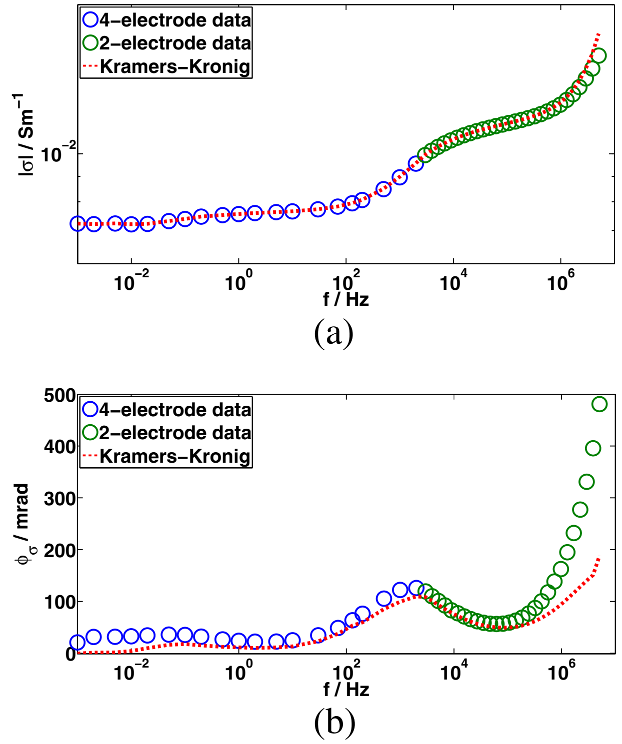

(a)

(b)

Fig. 12. Bode plot of combined data of concrete samples, measured by Reichling (2013). Four electrode data (blue circles), corrected two-electrode data (green circles) and Kramer–Kronig relations (dashed red line), cf. Table 1.

6. Conclusion and discussion

We provide a workflow for obtaining a meaningful wideband dielectric data set from 1 mHz to 10 MHz by combining four- and two-

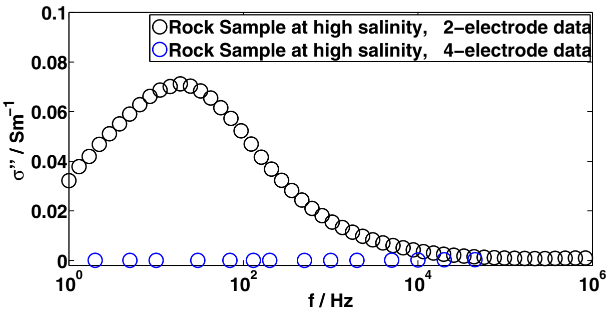

Fig. 13. Imaginary conductivity of a rock sample of very high saturating salinity of $\sigma_f \approx 22.2$ Sm^{-1} at $T = 20.6$ °C, two-electrode data (black circles) and four-electrode data (blue circles), cf. Table 1. The dispersive error of the two-electrode measurement remains irreducibly high within the frequency overlap of the two instruments.

electrode data. Doing so, we remove non-sample dispersion effects, present in the original data sets. By using the two measurements for mutual verification, we are able to correct the data without necessity to first quantitatively describe or even correct the physical mechanisms of disturbance. As precondition, a frequency (range) of mutual confirmation of imaginary conductivity data must exist in the overlapping frequency range of the two setups. We assess the quality of our procedures in terms of mathematical consistence and simple physical models. Moreover, we show that our approach is superior to other correction approaches.

The method was proven on water samples of slightly different conductivity, where the corrected data exactly match the simulated (water) dispersion curve. Applicability was shown for different porous media. Our procedure offers the possibility to eventually repeat a particular smaller part of the frequency range, since a correction procedure for small deviations, which will appear due to a time lag between repeats, is already part of the standard processing.

A drawback of the proposed method might result from a required point of negligible dispersive errors at a mutual frequency for both instruments, which are not necessarily present, e.g. for highly conductive samples. These cases would require subsequent-correction methods as intermediate step, which were otherwise avoided. Additionally, one should consider replacing the instrument compensation at highest available frequencies (~MHz), which is still an error source for highest precision, and instead further enhance the frequency range using the proposed method with an additional experimental setup, e.g. network analyzers with coaxial probe or transmission line techniques, up to GHz range.

Acknowledgments

The presented study was supported by the German Society for Petroleum and Coal Science and Technology (DGMK 703) — in particular by its members ExxonMobil Production Deutschland GmbH, GDF SUEZ E&P Deutschland GmbH, RWE Dea AG and Wintershall Holding GmbH — in the framework of the DGMK project 703 “IS for assessing the wetting conditions of reservoir rocks”. Additional support was provided by the Transregional Collaborative Research Center 32 (TR32/2), funded by the German Research Foundation (DFG). The authors thank L. Ahrensmeier, M. Penz and T. Houben and C. Bobe for assistance during measurements and K. Reichling for testing our procedures in the framework of his research.

References

Archie, G., 1942. The electrical resistivity log as an aid in determining some reservoir characteristic. Trans. Am. Inst. Min. Metall. Pet. Eng. 146, 54–62.
Börner, F., Schopper, J., Weller, A., 1996. Evaluation of transport and storage properties an the soil and groundwater zone from induced polarization measurements. Geophys. Prospect. 44, 583–601.
Bücker, M., Hördt, A., 2013. Long and short narrow pore models for membrane polarization. Geophysics 78 (6), E299–E314.
Cao, W., Gerhardt, R., 1990. Calculation of various relaxation times and conductivity for a single dielectric relaxation process. Solid State Ionics 42 (3), 213–221.
Chelidze, T., Guegen, Y., 1999. Electrical spectroscopy of porous rocks: a review—I. Theoretical models. Geophys. J. Int. 137, 1–15.
Cole, K., Cole, R., 1941. Dispersion and absorption in dielectrics. I. Alternating current characteristics. J. Chem. Phys. 9, 341–351.
Cosenza, P., Ghorbani, A., Camerlynck, C., Rejiba, F., Guérin, R., Tabbagh, A., 2009. Effective medium theories for modelling the relationships between electromagnetic properties and hydrological variables in geomaterials: a review. Near Surf. Geophys. 7 (5–6), 563–578.
Dias, C., 2000. Developments in a model to describe low-frequency electrical polarization of rocks. Geophysics 65 (2), 437–451.
Esteban, J., Orazem, M., 1991. On the application of the Kramers–Kronig relations to evaluate the consistency of electrochemical impedance data. J. Electrochem. Soc. 138 (1), 67–76.
Fehr, A., 2007. NMR- und SIP-Messungen an Gesteinsproben. (Diploma thesis). RWTH Aachen University, Aachen, Germany.
Gerhardt, R., 1994. Impedance and dielectric spectroscopy revisited: distinguishing localized relaxation from long-range conductivity. J. Phys. Chem. Solids 55 (12), 1491–1506.
Hanai, T., 1960. Theory of the dielectric dispersion due to the interfacial polarization and its application to emulsions. Kolloid-Z. 171 (1), 23–31.
Kavian, M., 2011. Electric Characterization of Layered Sand and Clay Under Continuous Fluid Flow Conditions: Experiments and Data Analysis for Frequencies Between 100 kHz and 3 MHz. (PhD thesis). Delft University of Technology, Delft, Netherlands.
Kemna, A., Binley, A., Cassiani, G., Niederleithinger, E., Revil, A., Slater, L., Williams, K., Orozco, A., Haegel, F.-H., Hoerdt, A., Kruschwitz, S., Leroux, V., Titov, K., Zimmermann, E., 2012. An overview of the spectral induced polarization method for near-surface applications. Near Surf. Geophys. 10 (6), 453–468.
Klein, L., Swift, C., 1977. An improved model for the dielectric constant of sea water at microwave frequencies. IEEE Trans. Antennas Propag. 25 (1), 104–111.
Lockner, D., Byerlee, J., 1985. Complex resistivity measurements of confined rock. J. Geophys. Res. Solid Earth 90 (B9), 7837–7847 (1978–2012).
Marshall, D., Madden, T., 1959. Induced polarization, a study of its causes. Geophysics 24 (4), 790–816.
Maxwell, J., 1873. A Treatise on Electricity and Magnetism vol. I. Clarendon Press, Oxford, UK.
McKubre, M., Macdonald, D., Macdonald, J., 1987. Impedance spectroscopy. Emphasizing Solid Materials and Systems. John Wiley & Sons (Ch. 3.1.2.9).
Nordsiek, S., Weller, A., 2008. A new approach to fitting induced-polarization spectra. Geophysics 73 (6), F235–F245.
Pelton, W., Ward, S., Hallof, P., Sill, W., Nelson, P., 1978. Mineral discrimination and removal of inductive coupling with multifrequency IP. Geophysics 43 (3), 588–609.
Reichling, K., 2013. Bestimmung und Bewertung des elektrischen Widerstandes von Beton mit geophysikalischen Verfahren. (PhD Thesis). Faculty of Civil Engineering, RWTH Aachen University, Aachen, Germany.
Revil, A., 2013. Effective conductivity and permittivity of unsaturated porous materials in the frequency range 1 mHz–1 GHz. Water Resour. Res. 49 (1), 306–327.
Revil, A., Florsch, N., 2010. Determination of permeability from spectral induced polarization in granular media. Geophys. J. Int. 181, 1480–1498.
Schwarz, G., 1962. A theory of the low-frequency dielectric dispersion of colloidal particles in electrolyte solution. J. Phys. Chem. 66 (12), 2636–2642.
Slater, L., 2007. Near surface electrical characterization of hydraulic conductivity: from petrophysical properties to aquifer geometries—a review. Surv. Geophys. 28 (2–3), 169–197.
Titov, K., Komarov, V., Tarasov, V., Levitski, A., 2002. Theoretical and experimental study of time domain-induced polarization in water-saturated sands. J. Appl. Geophys. 50, 417–433.
Volkmann, J., Klitzsch, N., 2010. Frequency-dependent electric properties of microscale rock models for frequencies from one millihertz to ten kilohertz. Vadose Zone J. 9 (4), 858–870.
Volkmann, J., Klitzsch, N., Mohnke, O., Schleifer, N., 2013. Rock properties influencing impedance spectra (IS) studied by lab measurements on porous model systems (extended abstract). Proceedings: International Symposium of the Society of Core Analysts Held in Napa Valley, California, USA, 16–19 September, 2013, pp. 419–424.
Wagner, K., 1914. Erklärung der dielektrischen Nachwirkunsvorgänge auf Grund Maxwellscher Vorstellungen. Arch. Elektr. 2 (9), 371–387.
Zimmermann, E., 2010. Phasengenaue Impedanzspektroskopie und -tomographie für geophysikalische Anwendungen. (PhD thesis). Faculty of Mathematics and Natural Sciences, Rheinische Friedrich-Wilhelms-Universität Bonn, Bonn, Germany.
Zimmermann, E., Kemna, A., Berwix, J., Glaas, W., Münch, H., Huisman, J., 2008. A high-accuracy impedance spectrometer for measuring sediments with low polarizability. Meas. Sci. Technol. 19 (10), 105603.